Hydrogen dissociation on metal surfaces: A semi-empirical approach

Nour Ghassemi, E.

CHAPTER 5

Transferability of the Specific Reaction Parameter Density Functional for H_2 + Pt(111) to H_2 + Pt(211)

This chapter is based on:

Elham Nour Ghassemi, Egidius W. F. Smeets, Mark F. Somers, Geert-Jan Kroes, Irene M. N. Groot, Ludo B. F. Juurlink, and Gernot Füchsel. The Journal of Physical Chemistry C **123**(5), 2973-2986, 2019.

Abstract

The accurate description of heterogeneously catalyzed reactions may require the chemically accurate evaluation of barriers for reactions of molecules at edges of metal nanoparticles. It was recently shown that a semi-empirical density functional describing the interaction of a molecule dissociating on a flat metal surface (CHD_3 + Pt(111)) is transferable to the same molecule reacting on a stepped surface of the same metal (Pt(211)). However, validation of the method for additional systems is desirable. To address the question whether the specific reaction parameter (SRP) functional that describes H_2 + Pt(111) with chemical accuracy is capable of also accurately describing H_2 + Pt(211), we have performed molecular beam simulations with the quasi-classical trajectory (QCT) method, using the SRP functional developed for H_2 + Pt(111). Our calculations used the Born-Oppenheimer static surface (BOSS) model. The accuracy of the QCT method was assessed by comparison with quantum dynamics (QD) results for reaction of the ro-vibrational ground state of H_2. The theoretical results for sticking of H_2 and D_2 on Pt(211) are in quite good agreement with experiment, but uncertainties remain due to a lack of accuracy of the QCT simulations at low incidence energies, and possible inaccuracies in the reported experimental incidence energies at high energies. We also investigated the non-adiabatic effect of electron-hole pair excitation on the reactivity using the molecular dynamics with electronic friction (MDEF) method, employing the local density friction approximation (LDFA). Only small effects of electron-hole pair excitation on sticking are found.

5.1 Introduction

The heterogeneous catalysis community is highly interested in stepped surfaces because structure-sensitive catalyzed reactions often occur at edges of nanoparticles. These edges contain low-coordinated surface atoms, which resemble the atoms present at step edges of stepped surfaces. Consequently, a number of experiments have addressed dissociative chemisorption reactions of molecules on stepped surfaces, such as NO at steps on defective Ru(0001) [1], H_2 on stepped Pt surfaces [2–8], N_2 at steps on defective

Ru(0001) [9, 10], and methane on Pt surfaces [11, 12], to name but a few examples. A much lower number of theoretical dynamics studies have addressed dissociative chemisorption on stepped surfaces, and these studies have looked at H_2 + Pt(211) [13–17] , H_2 + Cu(211) [18, 19], H_2 dissociation on defective Pd(111) [20], and at CHD_3 + Pt(211) [12, 21–24].

In view of the importance of dissociative chemisorption reactions on stepped surfaces to heterogeneous catalysis, it would obviously be useful to have a predictive procedure in place for accurately evaluating the interaction between a molecule and a stepped surface. Recent experimental work suggests that such a procedure may be based on experiments and dynamics calculations based on semi-empirical density functional theory (DFT) for the electronic structure, for the same molecule interacting with a low-index, flat surface of the same metal [12]. As has now been established for several systems, dynamics calculations based on electronic structure calculations with the specific reaction parameter approach to DFT (SRP−DFT) are able to reproduce sticking measurements on such systems with chemical accuracy [12, 25–28]. Very recently, it has been shown that the SRP density functional (SRP−DF) for CHD_3 interacting with the flat Pt(111) system is transferable to the same molecule interacting with the stepped Pt(211) system [12] (transferability of the SRP DF from H_2 + Cu(111) [12] to H_2 + Cu(100) [26], *i.e.*, among systems in which the same molecule interacts with different flat, low-index surfaces, had been established earlier [26]). However, this finding just concerned only one specific system, and it is important to check whether this finding also holds for other systems. The main goal of this work is to investigate whether the SRP−DF recently determined for H_2 + Pt(111) [28] is also capable of yielding chemically accurate results for H_2 + Pt(211).

The system of interest to our study (H_2 + Pt(211)) has first been studied theoretically. Olsen *et al.* [13] computed a six-dimensional (6D) potential energy surface (PES) for the system with DFT, using the GGA functional due to Becke [29] and Perdew [30] (BP), and interpolating the DFT results with the corrugation reducing procedure (CRP) [31]. They next performed classical trajectory studies on this PES within the Born-Oppenheimer and static surface (BOSS) approximations. On the basis of these calculations, they were able to show that a trapping mechanism contributes a component to the sticking probability which is high at low incidence energy (E_i) and decreases monotonically with E_i [13]. In this mechanism, H_2 gets trapped at an unreactive site, *i.e.*, at the bottom of the step, and then diffuses to

an atom at the top of the step edge, where it subsequently reacts.

Next, McCormack *et al.* also analyzed the other contributing mechanisms to the sticking of H_2 on Pt(211) [14]. Their classical trajectory calculations using the same PES as used before showed two additional mechanisms. A mechanism in which H_2 reacts directly at the step is non-activated and contributes equally at all E_i. In an additional mechanism, H_2 reacts on the terrace. In this mechanism the reaction is activated, yielding a contribution to the sticking that rises monotonically with increasing E_i. By scaling the contributions from the different mechanisms according to the different lengths of the (111) terraces in the Pt(211) and Pt(533) surfaces (both exhibiting (111) terraces and (100) steps), they [14] were able to obtain good agreement with previous experiments on H_2 + Pt(533) [6].

In two subsequent studies using the same PES, Luppi *et al.* [15] investigated rotational effects with classical trajectory calculations, while Olsen *et al.* [17] made a comparison between quantum dynamics and classical dynamics results for reaction of ($\nu = 0$, $j = 0$) H_2. According to the classical trajectory studies of Luppi *et al.*, the trapping-mediated contribution to the reaction, which leads to a high sticking probability at low E_i, but which contribution then quickly decreases with E_i, should be present for low rotational states ($j = 0$ and 1), but should disappear for states with intermediate j. The reason they provided is that energy transfer to rotation should cause trapping for $j = 0$ and $j = 1$, while energy transfer from rotation should instead hinder trapping. Olsen *et al.* found that QCT calculations were in good agreement with quantum dynamics results for high E_i (in excess of 0.1 eV). However, the QCT study overestimated the trapping-mediated contribution to the reaction at low E_i, which was attributed to one mechanism operative for trapping in the classical calculations (excitation of the rotation) not being allowed in quantum dynamics, as the trapping well should not support rotationally excited bound states for their PES [17].

H_2 + Pt(211) has also been studied experimentally by Groot *et al.* [7, 8, 32]. Their molecular beam sticking probabilities [7] were in reasonable agreement with the quantum dynamics results for ($\nu = 0$, $j = 0$) H_2 of Olsen *et al.* [17], although the quantum dynamics results based on the BP functional overestimated the sticking at high E_i. Likewise, there were discrepancies at low E_i, with the computed trapping-mediated contribution to the sticking being too low compared to the experimental result. In two subsequent papers, Groot *et al.* showed that the sticking on surfaces with longer (111) terraces and (100) steps (Pt(533) and Pt(755)) can successfully

be modeled based on the contributing mechanisms to sticking at the step and at the terrace on Pt(211) [8, 32], much like McCormack *et al.* had done before for Pt(533) [14]. They also used their results to analyze the contributions of facets and edges of Pt nanoparticles to H_2 dissociation proceeding on these nanoparticles [8].

The goal of this chapter is to test whether the SRP−DF for H_2 + Pt(111) is transferable to H_2 + Pt(211). For this reason, we will put emphasis on the comparison of sticking probabilities computed with a PES obtained with the SRP−DF for H_2 + Pt(111) with the experimental results of Ref. [8], taking the experimental conditions (velocity distributions of the beams, nozzle temperatures T_n used) into account as fully as possible. Our calculations are done within the BOSS model, and mainly use the QCT method for the dynamics. We will not reanalyze the mechanisms contributing to the reaction, simply noting that the dependence of the computed sticking probabilities on E_i is in accordance with conclusions arrived at earlier by Olsen *et al.* [13] and McCormack *et al.* [14] . We find that, overall, the computed sticking probability is in good agreement with experiment for both H_2 and D_2 + Pt(211), suggesting that the transferability may well hold. However, at present this conclusion is not yet certain due to uncertainties in the parameters needed to describe the molecular beams used in the experiments. Our results suggest that, once more precisely defined experimental results become available, the comparison with experiment should be revisited on the basis of quantum dynamics calculations.

This chapter is set up as follows. Section 5.2.1 describes the dynamical model, and Section 5.2.2 and Section 5.2.3 describe the construction of the PES and the PES interpolation method. The dynamics methods used here are explained in Section 5.2.4 and Section 5.2.5. Section 5.2.6 describes how we calculate the observables. Section 5.2.7 provides computational details. In Section 5.3, the results of the calculations are shown and discussed. Section 5.3.1 describes the computed PES. In Section 5.3.2, we compare the QCT results with the QD results. The isotope effect of the QCT results for reaction of ($\nu = 0, j = 0$) H_2 and D_2 is shown and discussed in Section 5.3.3. Section 5.3.4 provides theoretical results on molecular beam sticking probabilities and comparison with the experimental data. In Section 5.3.5, the effect of electron-hole pair excitation on the reactivity is discussed and the MDEF results are compared with the MD results for sticking. Conclusions are provided in Section 5.4.

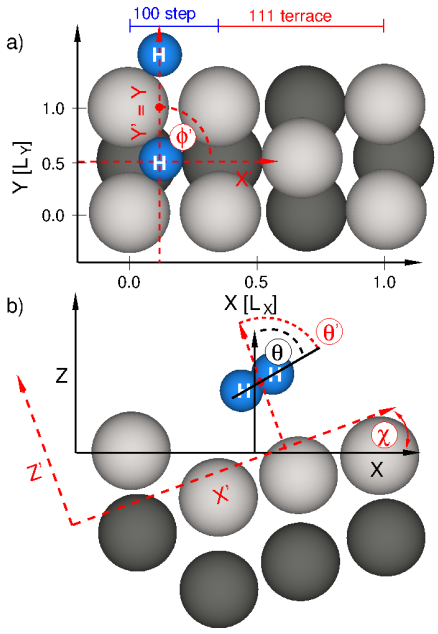

Figure 5.1: Coordinate systems for H_2 on Pt(211). (a) Top view of the (1×1) unit cell showing also the dissociated reference geometry of H_2 used to converge the computational setup with respect to the adsorption energy E_{ads}. First and second layer Pt atoms are in silver and dark gray, respectively. H atoms are blue colored. (b) Side view of the slab model. The Z-axis (molecule-surface distance) in the standard coordinate system drawn in black is aligned with the normal to the macroscopic surface. X and Y are the lateral components of the COM position of H_2 indicated by a red dot. Furthermore, r is the interatomic H−H distance (not shown) and the angular orientation is specified by the polar angle $\theta \in [0, \pi]$ and the azimuthal angle $\phi \in [0, 2\pi]$ (not shown). The angular orientation of H_2 in the internal coordinate system is defined with respect to the normal of the (111) terrace, as shown in red. The two coordinate systems include an angle χ of 20°. The corresponding angular coordinates are $\{\theta', \phi'\}$. The surface lattice constants are $L_X = 6.955$ Å and $L_Y = 2.839$ Å.

5.2 Theoretical methodology

5.2.1 Dynamical model

The dynamics simulations presented in the following approach the true reaction dynamics of the system by assuming the reaction to take place on an ideal rigid Pt(211) surface at zero coverage. During the entire dynamics, the surface atoms are fixed at their initial equilibrium positions as obtained from DFT calculations. The dynamical degrees of freedom (DOF) treated here are the six DOF of H_2. These are the center-of-mass (COM) position given by Cartesian coordinates X, Y, Z relative to a surface atom, the interatomic H−H distance r and the angular orientation of the molecule defined with respect to the macroscopic surface plane. As usual, X, Y are the lateral components of the COM position and Z is the molecule-surface distance. The orientation of the molecule is specified by the polar angle $\theta \in [0, \pi]$ and the azimuthal angle $\phi \in [0, 2\pi]$. The corresponding coordinate system is visualized in Figure 5.1.

5.2.2 Electronic structure calculations

In this work, electronic structure calculations are carried out using periodic DFT as implemented in the *Vienna Ab Initio Simulation Package* (VASP) [33–36]. Specifically, we employ an exchange-correlation functional of the form:

$$E_{XC} = E_X^{PBE\alpha} + E_C^{vdW-DF2} \tag{5.1}$$

which contains PBEα exchange [37] and the vdW-DF2-functional of Lundquist and Langreth and co-workers [38]. The latter accounts for long-range van der Waals interactions. The α-value was set to 0.57 according to our previous work [28] where we have determined this value to be suitable in order to bring computed and measured [39] sticking probabilities for D_2 on Pt(111) in quantitative agreement, see also Chapter 3. At first sight, the strategy of fitting a DFT functional to an experiment performed on a particular system might lead to a functional that is too specific to be accurate also for other systems, even though they might appear very similar chemically. However, recent theoretical work on the dissociation of molecular hydrogen on different facets of Cu [25, 26] and methane dissociation on nickel [27] and platinum [12] surfaces have shown that so-optimized functionals may indeed be transferable among different but chemically similar systems. This sug-

gests that the SRP functional designed for the D_2 + Pt(111) system might be of similar accuracy for the $D_2(H_2)$ + Pt(211) system.

The DFT calculations on the D_2 + Pt(211) system presented here are based on a Pt(211) slab model with four layers using a (1×2) supercell. As often done for hydrogen + metal systems, we here assume effects resulting from surface atom motion on the dissociation dynamics to be negligible at the relevant experimental conditions to which we will compare our simulations. Consequently, we content ourselves with a representation of the interaction potential for a frozen Pt(211) surface. The surface atom positions of the three uppermost layers are initially optimized by relaxing the Pt slab, but then kept frozen for all subsequent calculations on the system. We took care that the mirror axis was not affected by the geometry optimization of the slab. The resulting slab model obeys the symmetry of the $p1m1$ plane group [18]. This is helpful in reducing the computational burden associated with the construction of the 6D PES, as we will show below. Similar to Ref. [18], the vacuum gap separating periodic slab images is about 16.2 Å. We use a Γ−centered 7×7×1 k-point mesh generated according to the Monkhorst grid scheme [40]. The energy cut-off, E_{PAW}, used in the projector augmented wave (PAW) method was set to 450 eV. We employ Fermi smearing with a width of 0.1 eV. The optimal number of k-points and surface layers, and the optimal E_{PAW} value were determined by convergence calculations as summarized in table 5.1. There, we list the adsorption energy E_{ads} computed as difference between the minimum energy of H_2 at its equilibrium distance $r_{eq} \approx 0.74$ Å in the gas phase (here about 6 Å away from the surface, and parallel to the surface) and the dissociatively adsorbed configuration of H_2 on Pt(211) as depicted in Figure 5.1. E_{ads}-values are listed in table 5.1 for different slab thicknesses, k-point meshes, and cut-off energies. The lattice constants of the rectangular (1×1) surface unit cell are $L_X = 6.955$ Å along the X-axis and $L_Y = 2.839$ Å along the Y-axis, corresponding to a bulk lattice constant D of 4.016 Å. The latter value compares reasonably well with the experimental value ($D = 3.916$ Å [41]).

5.2.3 Representation of the potential energy surface

In order to construct a continuous electronic ground state PES for molecular hydrogen interacting with a rigid Pt(211) system, we adopt the CRP [31] which allows for a fast and accurate interpolation of DFT data points. The

Table 5.1: Adsorption energies E_{ads} in eV for H_2 on Pt(211) computed using different k-point meshes, cut-off energies E_{PAW} and number of layers in the slab. The E_{ads}-value obtained with a converged computational setup is marked by an asterisk. The reference geometry of dissociated H_2 used to determine E_{ads} is shown in Figure 5.1.

	4 layer slab				**5 layer slab**			
$\mathbf{E_{PAW}}$ **[eV]**	350	400	450	500	350	400	450	500
5×5×1	0.951	0.940	0.934	0.931	0.951	0.939	0.934	0.931
6×6×1	0.952	0.941	0.935	0.932	0.951	0.940	0.934	0.931
7×7×1	0.962	0.952	0.945*	0.943	0.962	0.951	0.945	0.942
8×8×1	0.963	0.953	0.947	0.944	0.953	0.952	0.946	0.943

six-dimensional PES accounts only for the six DOF of molecular hydrogen as shown in Figure 5.1. Details about the CRP algorithm and its implementation in our in-house computer code are presented elsewhere [18]. In the following, only a few principles of the CRP will be explained, and a few details will be presented concerning the structure of the DFT data set. The interpolation of realistic globally defined PESs can become considerably error-prone when small geometrical alterations lead to strong changes of the system's potential energy. Using the CRP, this problem can be avoided by first reducing large differences within the original DFT data points, V^{DFT}. The resulting reduced data set, I^{DFT},

$$I^{DFT}(\vec{Q}_i) = V^{DFT}(\vec{Q}_i) - V^{ref}(\vec{Q}_i) \tag{5.2}$$

is better suited for an interpolation which will yield the smooth function $I(\vec{Q})$ used to compute the final PES according to:

$$V(X, Y, Z, r, \theta, \phi) := V(\vec{Q}) = I(\vec{Q}) + V^{ref}(\vec{Q}). \tag{5.3}$$

Here, $\vec{Q}_i = (X_{i_1}, Y_{i_2}, Z_{i_3}, r_{i_4}, \theta_{i_5}, \phi_{i_6})^T$ is a discrete coordinate vector, labeled with the multidimensional index i, in the 6D space $\vec{Q} = (X, Y, Z, r, \theta, \phi)^T$. For the reference function, $V^{ref}(\vec{Q})$, we are here using the sum of the two H + Pt(211) interaction potentials which are also obtained via the CRP. They describe most of the repulsive features of the PES, and are therefore

particularly suitable for reducing the corrugation of the PES in the CRP as explained in Ref. [18] and Ref. [31].

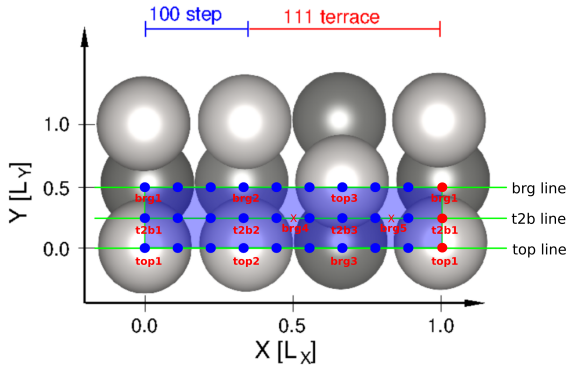

Figure 5.2: Top view of a (1 × 1) unit cell of Pt(211). Indicated is the irreducible wedge by a blue plane and the blue dots represent the positions of H and of the center of mass of H_2, respectively, at which DFT energy points were calculated in order to construct the 3D/6D PES. A few selected sites are labeled with top, brg (bridge) and t2b (top to bridge) and are further distinguished by numbers. Red dots indicate periodic images at the edge of the irreducible wedge.

In order to keep the number of DFT points to be computed as low as possible, we perform DFT calculations for specific angular orientations of H_2 labeled by $\{\theta', \phi'\}$ in the following. They are defined in a modified coordinate system which is aligned with the vector normal to the (111) terrace, and not with the vector normal to the macroscopic surface as is the case for the angular coordinates $\{\theta, \phi\}$. The corresponding transformations between the two coordinate systems were previously presented in the supplementary information of Ref. [18] and in Ref. [42]. In tables 5.2 and 5.3, we list details about the DFT grid representation of the PES for the H(D) + Pt(211) system as well as for the $H_2(D_2)$ + Pt(211) system. The former is required to provide the reference PES $V^{ref}(\vec{Q})$ in Equations (5.2) and (5.3). Note that, with the coordinate system chosen for the DFT calculations, for H + Pt(111) a low minimum value of Z is needed to map out the interaction of H with Pt(211) at the bottom of the step (see table 5.2). In

Table 5.2: Specification of the DFT grid used to represent the atomic reference H + Pt(211) interaction potential. The grid along Y is defined for the irreducible wedge (IW) which makes up only the half of the Pt(211)(1×1) unit cell, see Figure 5.2.

quantity	**value**	**unit**	**remark**
grid range along X on IW	$[0, L_X[$	Å	
grid range along Y on IW	$[0, L_Y/2]$	Å	
grid range along Z	[-3.65, 7.05]	Å	
N_X number of grid points in X on IW	18		equidistant
N_Y number of grid points in Y on IW	3		equidistant
N_Z number of grid points in Z	109		equidistant
ΔX grid spacing along X	$L_X/18$	Å	
ΔY grid spacing along Y	$L_Y/4$	Å	
ΔZ grid spacing along Z	0.1	Å	
representation of V^{top} reference potential			
grid range along Z	[0, 7.05]	Å	
N_Z^{top} number of grid points in Z	576		non-equidistant

the CRP, this is required in order to remove the repulsive interaction in the H_2 + Pt(211) PES over the whole interpolation range before interpolation is carried out. Due to the (100) step, the surface roughness is increased and small molecule-surface distances need to be taken into account (here, Z_{min} = -2.2 Å.). The reasons are that we also describe molecular configurations in which H_2 stands perpendicular to the surface and that we represent large interatomic distances (r_{max} = 2.5 Å.), atomic repulsions must then also be represented for small atom-surface distances, down to Z = -3.45 Å.

We apply the following interpolation order to generate a smooth function $I^{DFT}(\vec{Q})$. First, we interpolate along the interatomic H−H distance r and the molecule-surface distance Z using a two-dimensional spline interpolation. Second, we interpolate along the polar angle θ' using a trigonometric interpolation. Finally, we interpolate along the lateral positions X, Y and the azimuthal angle ϕ' using a symmetry-adapted three-dimensional Fourier interpolation. The resulting PES is smooth, fast to evaluate and provides analytical forces.

5.2.4 Molecular dynamics simulations

In this chapter, the dissociation dynamics of molecular hydrogen on Pt(211) is modeled using the QCT method [43], *i.e.*, with molecular dynamics (MD) simulations. The quantum mechanical ro-vibrational energy of incident H_2/D_2 is sampled by a Monte-Carlo procedure outline in Ref. [44] and the occupation of the associated ro-vibrational levels is determined by the molecular beam parameters, as discussed below. We distinguish between standard MD simulations and molecular dynamics simulations with electronic friction (MDEF) [45]. The latter method allows one to study non-adiabatic effects on the dissociation dynamics due to the creation of electron-hole pairs in the surface region. For a N-dimensional system, the general equation to be solved in the following is the Langevin equation [46] which reads:

$$-m_i \frac{d^2 q_i}{dt^2} = -\frac{\partial V(q_1, \ldots, q_N)}{\partial q_i} - \sum_j \eta_{ij}(q_i, \ldots, q_N) \frac{dq_i}{dt} + R(T). \qquad (5.4)$$

Here, m_i is the mass associated with a generalized coordinate q_i, η_{ij} is an element of the friction tensor which yields a dissipative term due to the coupling of the nuclear DOF of molecular hydrogen with the electronic DOF of the Pt(211) surface. Finally, $R(T)$ is a white noise random force

Table 5.3: Specification of the DFT grid used to represent the $H_2(D_2)$ + Pt(211) interaction potential. The grid along Y is specified for the irreducible wedge which equals here the lower half of the Pt(211)(1×1) unit cell, see Figure 5.2. Due to symmetry, the ϕ'-dependence of the PES along the *top* and the *brg* line can be represented with three points (here at $\phi' = 0, 45$ and 90°). Due to the absence of a mirror axis associated with the *t2b* line, we needed an additional point (here at $\phi' = 315°$) to sample the PES along ϕ'.

quantity	**value**	**unit**	**remark**
range of X	[0, L_X[	Å	
range of Y	[0,$L_Y/2$]	Å	
range of Z	[-2.2, 6.6]	Å	
range of r	[0.4, 2.5]	Å	
range of θ'	[0, $\pi/2$]	rad	
range of ϕ'	[-$\pi/4$, $\pi/2$]	rad	
N_X number of grid points along X	9		equidistant
N_Y number of grid points along Y	3		equidistant
N_Z number of grid points along Z	53		equidistant
N_r number of grid points along r	22		equidistant
$N_{\theta'}$ number of grid points along θ'	2		equidistant
$N_{\phi'}$ number of grid points along ϕ'	3-4$^{(*)}$		equidistant
ΔX grid spacing of X	$L_X/9$	Å	
ΔY grid spacing of Y	$L_Y/4$	Å	
ΔZ grid spacing of Z	0.15	Å	
Δr grid spacing of r	0.1	Å	
$\Delta\theta'$ grid spacing of θ'	$\pi/2$	rad	
$\Delta\phi'$ grid spacing of ϕ'	$\pi/4$	rad	

resulting from the electronic bath at temperature $T := T_{el} = T_s$, which here corresponds to the surface temperature T_s. At $T = 0$ K , the random force disappears and only the frictional force remains in the dissipative part of Equation (5.4). In the absence of electronic friction ($\eta = 0$), the Langevin equation obeys Newton's equation of motion and the evolution of the system depends then only on the gradient of the PES. The methodology used to

solve Equation (5.4) is described in Refs. [44, 47].

The position-dependent friction coefficients in Equation (5.4) are computed using the local-density friction approximation (LDFA) with the use of the independent atom approximation (IAA) [48]. As a consequence only the diagonal elements of the friction tensor $\underline{\underline{\eta}}$ remain and off-diagonal elements vanish. In the LDFA model, η is a function of the electron density $\rho(x, y, z)$ embedding the ion with position (x, y, z). In accordance with previous results [49], we assume that the embedding density corresponds to a good approximation to the unperturbed electron density of the bare Pt(211) surface which is here obtained from a single DFT calculation. To compute the friction coefficient for the H(D) atom, we adopt the relation [44]

$$\eta^{LDFA}(r_s) = a r_s^b \exp(-c r_s), \tag{5.5}$$

where the parameters are $a = 0.70881\ \hbar/a_0^{b+2}$, $b = 0.554188$, $c = 0.68314\ a_0^{-1}$ and were previously fitted in Ref. [44] to *ab initio* data [50]. The Wigner-Seitz radius $r_s = (3/(4\pi\rho))^{1/3}$ depends on the density $\rho(x, y, z)$ embedding the hydrogen at position (x, y, z). It is convenient to solve Equation (5.4) in Cartesian coordinates, and to use proper coordinate transformations to compute the potential and forces as functions of the six molecular coordinates presented in Figure 5.1.

Following previous studies on the reactive scattering of diatomic molecules from metal surfaces [44, 51], the effect of electron-hole pair excitation on the reaction of $H_2(D_2)$ on Pt(211) can also be studied by scaling the LDFA-IAA friction coefficients. Here, we consider a scaling factor of 1 ($\eta = \eta^{LDFA}$) and 2 ($\eta = 2 \times \eta^{LDFA}$). We investigate what happens if the friction coefficients are multiplied by a factor two because the LDFA-IAA friction model is approximate, ignoring the possible effects of the electronic structure of the molecule. Friction coefficients computed with the orbital dependent friction model tend to come out larger [52–54]. In the former case we have performed calculations for $T_s = T_{el} = 0$ K and 300 K, while in the latter case, we only performed calculations at $T_s = T_{el} = 0$ K, that is, in the absence of random forces.

5.2.5 Quantum dynamics simulations

Six-dimensional quantum dynamics calculations are performed with the time-dependent wave packet method [55, 56] using our in-house wave packet

propagation code by solving the time-dependent Schrödinger equation

$$i\hbar\frac{d\Psi(\vec{Q};t)}{dt} = \hat{H}\Psi(\vec{Q};t). \tag{5.6}$$

Here, $\Psi(\vec{Q};t)$ is the corresponding nuclear wave function of molecular hydrogen at time t. The Hamilton operator used in Equation (5.6) accounts for the motion in the six molecular DOF of H_2 and reads:

$$\hat{H} = -\frac{\hbar^2}{2M}\vec{\nabla}^2 - \frac{\hbar^2}{2\mu}\frac{\partial^2}{\partial r^2} + \frac{\hbar^2}{2\mu r^2}\hat{J}^2(\theta,\phi) + V(\vec{Q}), \tag{5.7}$$

where $\vec{\nabla}$ is the Nabla operator, and $\hat{J}(\theta,\phi)$ the angular momentum operator for the hydrogen molecule, M is the molecular mass and μ is the reduced mass of $H_2(D_2)$. The initial nuclear wave function is represented as a product of a wave function describing initial translational motion and a ro-vibrational eigenfunction $\Phi_{\nu,j,m_j}(r,\theta,\phi)$ of gaseous $H_2(D_2)$ characterized by the vibrational quantum numbers ν, the angular momentum quantum number j and the angular momentum projection quantum number m_j. Therefore, the initial wave function reads

$$\Psi(\vec{Q};t_0) = \psi(\vec{k_0},t_0)\ \Phi_{\nu,j,m_j}(r,\theta,\phi), \tag{5.8}$$

where $\vec{k_0} = (k_0^X, k_0^Y, k_0^Z)^T$ is the initial wave vector. The wave function describing initial translational motion is given by:

$$\psi(\vec{k_0},t_0) = e^{i(k_0^X X_0 + k_0^Y Y_0)}\int_{-\infty}^{\infty}\beta(k_0^Z)e^{ik_0^Z Z_0}dk_Z. \tag{5.9}$$

Here, the initial wave packet $\beta(k_0^Z)$ is characterized by a half-width parameter σ according to

$$\beta(k_0^Z) = \left(\frac{2\sigma^2}{\pi}\right)^{-\frac{1}{4}} e^{-\sigma^2(\overline{k}-k_0^Z)}e^{-i(\overline{k}-k_0^Z)Z_0}, \tag{5.10}$$

with $\overline{k}$ being the average momentum and Z_0 the position of the center of the initial wave packet.

The equations of motion were solved using the split-operator method [57]. The motion in X, Y, Z, and r was represented using Fourier grids. Quadratic optical potentials [58] were used to absorb the wave function at the edges

of the grid in r and Z. A non-direct product finite basis representation was used to describe the rotational motion of H_2 [59, 60]. To compute reaction probabilities, first S-matrix elements were computed for diffractive and ro-vibrationally elastic and inelastic scattering, using the scattering matrix formalism of Balint-Kurti *et al.* [61]. These were used to compute probabilities for diffractive and ro-vibrationally elastic and inelastic scattering. The sum of these probabilities yield the reflection probability, and substracting from 1 then yields the reaction probability.

5.2.6 Computation of observables

Using the quasi-classical method, we aim to model the sticking of $H_2(D_2)$ on Pt(211) at conditions present in experiments we compare with by taking into account the different translational and ro-vibrational energy distributions characterizing the different molecular beams. At a nozzle temperature T_n, the probability P_{beam} of finding molecular hydrogen in a specific ro-vibrational state ν, j with a velocity $v + dv$ in the beam is:

$$P_{beam}(v, \nu, j; T_n)dv = P_{int}(\nu, j, T_n) \times f_{vel}(v; T_n)dv, \tag{5.11}$$

where the flux-weighted velocity distribution

$$f_{vel}(v; T_n)dv = Cv^3 \exp(-(v - v_s)^2/\alpha^2)dv \tag{5.12}$$

is normalized by a normalization constant C and characterized by a width parameter α and the stream velocity v_s. The ro-vibrational state distribution is given by

$$P_{int}(\nu, j, T_n) = \frac{w(j)F(\nu, j, T_n)}{\sum_{v',j' \equiv j(\mathrm{mod}\ 2)} F(\nu', j', T_n)}. \tag{5.13}$$

The weight $w(j)$ accounts for the different nuclear spin configurations of ortho- and para hydrogen molecules. For H_2, $w(j) = 1/4$ (3/4) for even (odd) j-values and, for D_2, $w(j) = 2/3$ (1/3) for even (odd) values of j. The function $F(\nu, j, T_n))$ is defined as

$$F(\nu, j, T_n) = (2j+1) \underbrace{\exp(-(E_{\nu,0} - E_{0,0})/k_B T_n)}_{\text{vibrational energy distribution}} \underbrace{\exp(-(E_{\nu,j} - E_{\nu,0})/0.8 k_B T_n)}_{\text{rotational energy distribution}}. \tag{5.14}$$

The appearance of a factor 0.8 in the rotational energy distribution reflects that rotational and nozzle temperatures assume the relation $T_{rot} = 0.8\ T_n$ due to rotational cooling upon expansion of the gas in the nozzle [62]. The experimental beam parameters for the H_2/D_2 + Pt(211) systems are listed in table 5.4 and table 5.5.

The quasi-classical initial conditions are prepared using a Monte Carlo procedure described in Ref. [44] and sample directly the probability distribution P_{beam}. The resulting probability P_i for dissociative adsorption, scattering and non-dissociative trapping of an ensemble of molecules is determined by the ratio:

$$P_i = \frac{N_i}{N}, \tag{5.15}$$

where N_i stands for the number of adsorbed, dissociated or trapped trajectories (N_{ads}, N_{diss}, N_{trap}) and N is the total number of trajectories computed for a specific energy point $\langle E_i \rangle$, where $\langle E_i \rangle$ denotes the average translational incidence energy of the molecule.

5.2.7 Computational details

The time-integration of Equation (5.4) is done in Cartesian coordinates using a time step of $\Delta t = 2.0\hbar/E_\mathrm{h}$ (≈ 0.0484 fs) with the stochastic Ermak-Buckholz propagator [64], which also works accurately in the non-dissipative case. Further technical details are given in Ref. [44, 47] . The maximal allowed propagation time for each trajectory is $t_f = 10$ ps. In the non-dissipative case, our QCT setup usually leads to an energy conservation error of smaller than 1 meV. All trajectories start at a molecule-surface distance of 7 Å and initially sample the ensemble properties of the experimental molecular beam, that is, we model the ro-vibrational state distribution according to the nozzle temperature as well as the translational energy distribution of the incidence beam. The parameters characterizing the molecular beam are given in table 5.4 and table 5.5 and details about their experimental determination are given in the supporting information of Ref. [63]. The initial conditions used in the quasi-classical simulations are determined using the Monte-Carlo algorithm explained in Ref. [44].

We compute N = 10,000 trajectories per energy point and count trajectories as dissociatively adsorbed if they assume an interatomic H−H distance larger than 2.5 Å during the dynamics. Scattered trajectories are characterized by a sign change in the Z-component of the total momentum vector

Table 5.4: Parameters used for the molecular beam simulations of H_2 on Pt(211). The parameters were obtained from fitting the experimental time-of-flight (TOF) data to equation 6 in the supporting information of Ref. [63]. For pure H_2 beams, we also provide n in $\langle E_i \rangle = nk_BT_n$ and the corrected average incidence energy $\langle E_{corr} \rangle = 2.7k_BT_n$.

	$\langle \mathbf{E_i} \rangle$ [eV]	$\mathbf{v_s}$ [m/s]	$\boldsymbol{\alpha}$ [m/s]	$\mathbf{T_n}$ [K]	n in $\langle \mathbf{E_i} \rangle = \mathbf{nk_BT_n}$	$\langle \mathbf{E_{corr}} \rangle$ [eV]
	0.004	626.5	55.9	293	–	–
	0.009	943.5	127.8	293	–	–
	0.013	1085.1	111.6	293	–	–
	0.014	1145.2	118.7	293	–	–
	0.025	1531.4	96.6	293	–	–
	0.035	1747.5	293.9	293	–	–
H_2	0.043	2031.2	80.6	293	–	–
	0.132	3392.1	578.0	500	3.07	0.116
	0.181	3959.8	690.8	700	3.00	0.163
	0.169	4009.0	185.2	1300	–	–
	0.233	4442.8	862.5	900	3.00	0.210
	0.282	4838.8	1022.9	1100	2.98	0.255
	0.338	5223.2	1215.6	1300	3.02	0.302
	0.413	5617.0	1535.8	1500	3.20	0.348
	0.454	5790.7	1711.3	1700	3.10	0.395

Table 5.5: Parameters used for the molecular beam simulations of D_2 on Pt(211). The parameters were obtained from fitting the experimental time-fo-flight (TOF) data to equation 6 in the supporting information of Ref. [63] . For pure D_2 beams, we also provide n in $\langle E_i \rangle = nk_BT_n$ and the corrected average incidence energy $\langle E_{corr} \rangle = 2.7k_BT_n$.

	$\langle \mathbf{E_i} \rangle$ [eV]	$\mathbf{v_s}$ [m/s]	$\boldsymbol{\alpha}$ [m/s]	$\mathbf{T_n}$ [K]	n in $\langle \mathbf{E_i} \rangle = \mathbf{nk_BT_n}$	$\langle \mathbf{E_{corr}} \rangle$ [eV]
$\mathbf{D_2}$	0.008	626.8	49.8	293	–	–
	0.027	1103.2	134.9	293	–	–
	0.040	1379.2	75.5	293	–	–
	0.054	1555.6	218.1	600	–	–
	0.076	1860.0	237.5	800	–	–
	0.110	2239.9	267.3	1100	–	–
	0.130	2430.7	311.9	500	3.03	0.116
	0.140	2531.1	294.5	1100	–	–
	0.234	3191.0	548.1	900	3.02	0.209
	0.276	3628.1	160.3	1300	–	–
	0.346	3814.8	772.0	1300	3.09	0.303
	0.457	4304.1	989.4	1700	3.12	0.395

and have to pass a molecule-surface distance of $Z_{sc} = 7.1$ Å. We call a trajectory trapped if the total propagation time of 10 ps is reached and neither dissociation nor scattering has occurred.

The dissociative chemisorption of $H_2(\nu = 0, j = 0)$ on Pt(211) is investigated quantum mechanically over a translational energy range of $E_i \in [0.05, 0.75]$ eV using two different wave packet propagations. The analysis line used to evaluate the scattered fraction of the wave packet was put at $Z_{start}^{CAP} = 6.6$ Å. This is a suitable value since the PES is r-dependent only for all values $Z \geq 6.6$ Å, so it allows representing the wave function on a smaller grid using N_Z points in Z for all channels but the channel representing the initial state (called the specular state, and represented on a larger grid called the specular grid, using $N_{Z_{spec}}$ points). These parameters, and other parameters discussed below, are presented in table 5.6.

The grids in Z start at $Z = Z_{start}$ and share the same grid spacing. The grid in r is described in a similar way by the parameters r_{start}, N_r, and Δr. The numbers of grid points used in X and Y (N_X and N_Y) are also provided, as are the maximum value of j and m_j used in the basis set (j_{max} and $m_{j_{max}}$). The optical potentials used (also called complex absorbing potentials (CAPs)) are characterized by the value of the coordinate at which they start and end, and the value of the kinetic energy for which they should show optimal absorption [58]; these values were taken differently for the regular and the specular grid in Z. The time step Δt used in the split operator propagation and the total propagation time t_f are also provided. The initial wave packet is centered on Z_0 and is constructed in such a way that 95% of the norm of the initial wave function is associated with kinetic energies in motion towards the surface between E_{min} and E_{max}, as also provided in table 5.6.

5.3 Results and discussion

5.3.1 Static DFT calculations

Before we come to the dynamics calculations, we here first present general features of the interaction potential of atomic and molecular hydrogen and a Pt(211) surface. In Figure 5.3, we plot the minimum potential energy values for atomic H assuming the optimal atom-surface distance Z over the full (1×1) unit cell. The resulting H-Pt(211) PES resembles the PES earlier developed by Olsen *et al.* [42] on the basis of DFT energy point

Table 5.6: Characterization of the two different wave packet (WP) calculations for $(\nu = 0, j = 0)H_2$ incident normally on Pt(211) for translational energies of $E_i \in [0.05,0.75]$ eV. Specified are the grid parameters for the wave function and the PES, and parameters defining the complex adsorbing potential in r and Z, the center position Z_0 of the initial wave packet, and the corresponding translational energy range E_i covered.

Property	**WP1**	**WP2**	**unit**
WP grid parameters			
Range of X	[0, L_X[	[0, L_X[	a_0
N_X grid points in X	36	36	
Range of Y	[0, L_Y[	[0, L_Y[	a_0
N_Y grid points in Y	12	12	
Range of Z	[-2.0,19.45]	[-2.0,17.10]	a_0
N_Z	144	192	
ΔZ	0.15	0.10	a_0
$N_{Z_{spec}}$	210	220	
Range of r	[0.80, 9.05]	[0.80, 7.85]	a_0
N_r	56	48	
Δr	0.15	0.15	a_0
$j_{max} = m_{j_{max}}$	22	32	
Complex absorbing potentials			
Z^{CAP} range	[12.55,19.45]	[12.50,16.90]	a_0
Z^{CAP} Optimum	0.05	0.08	eV
Specular grid			
Z^{CAP}_{spec} start	22.75	16.10	a_0
Z^{CAP}_{spec} end	29.35	19.90	a_0
Z^{CAP}_{spec} optimum	0.05	0.08	eV
r^{CAP} range	[4.10,9.05]	[4.55,7.85]	a_0
r^{CAP} optimum	0.05	0.20	eV
Propagation			
Δt	2.00	2.00	$\hbar/E_h$
t_f	3870.21	1741.60	fs
Initial wave packet			
Energy range, E_i	[0.05,0.25]	[0.20,0.75]	eV
Center of WP, Z_0	16.45	14.30	a_0

calculations using a B88P86 functional [29, 30]. For example, the most

stable adsorption site for a single hydrogen atom on Pt(211) is located near the brg1 position at the step edge, see also Figure 5.2. Additional minima are found close to the top2 and the top3 sites. In agreement with Olsen *et al.* [42], we also obtain the largest diffusion barrier to be ≈ 0.60 eV above the global minimum in the vicinity of the brg2 site. The specific position of the global minimum for H adsorption suggests the minimum barrier for H_2 dissociation to be on top of the step edge at the top1 site because the top1-to-brg1 path represents a short route for H atoms to assume their most

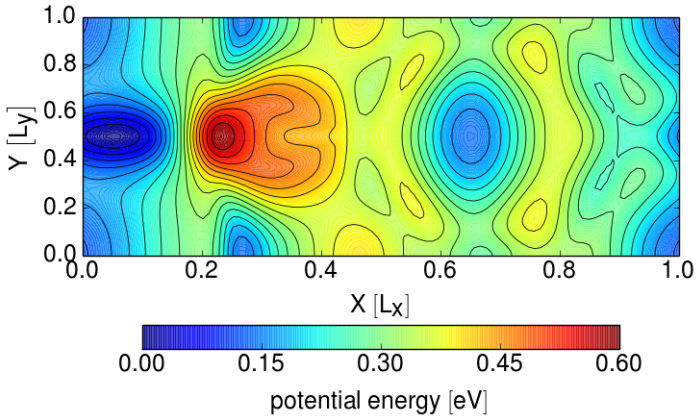

Figure 5.3: Minimum potential energy for H on Pt(211) for geometry optimized atom-surface distances Z_{opt} on a (1×1) supercell. The energies are given relative to the most stable configuration of H on Pt(211) which is here near to the brg1 position (see Figure 5.2). Since our DFT calculations do not include spin-polarization, the corresponding highest adsorption energy of 3.74 eV for a single H atom should to our experience be overestimated by ∼ 0.7 eV. The contour line spacing is 0.03 eV.

favorable geometry on the surface. In general, the abstraction of atomic hydrogen from Pt(211) requires large amounts of energies as is known also for other H + transition metal systems [65, 66]. The value of E_{ads} ≈ 3.7 eV computed here is, however, overestimated by ∼ 0.7 - 1.0 eV since we did not perform spin-polarized DFT calculations, which are not relevant to the comparison with the work of Olsen *et al.* [42], to the reaction paths for H_2 dissociation, and to the dynamics of H_2 dissociation.

In Figure 5.4, we present different two-dimensional (2D) PES cuts along

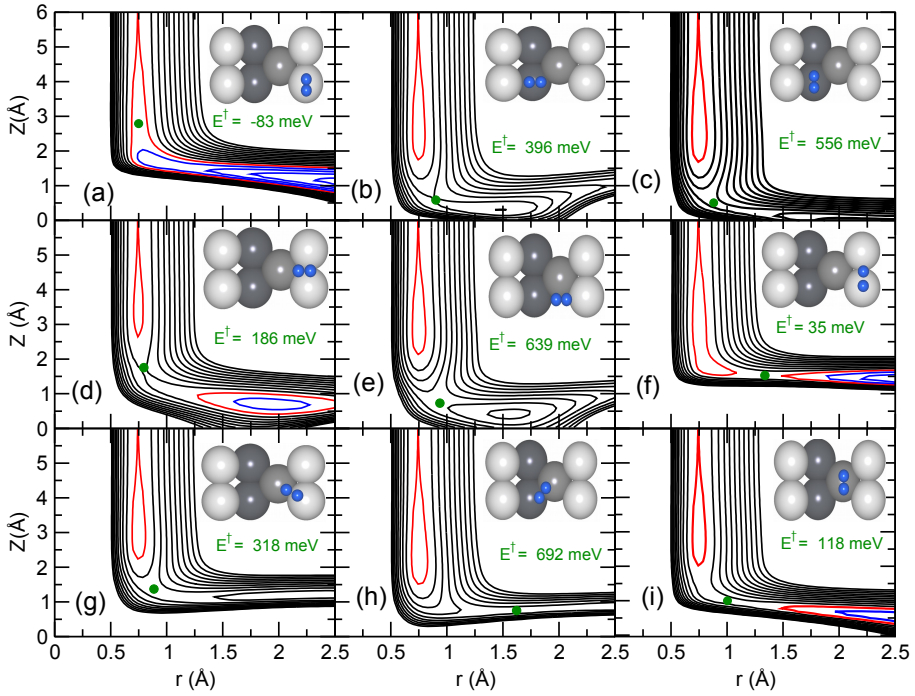

Figure 5.4: 2D potential cuts through the 6D PES for dissociative adsorption of H_2 on Pt(211) along r and Z at the nine different sites on the (1 × 1) unit cell. In all cases H_2 approaches parallel to the macroscopic surface ($\theta = 90°$). Top views of the molecular configurations are shown as insets. Contour levels are give in the energy range of [-1, 2] eV with a spacing of 0.2 eV. The zero-value of the PES is set equal to the gas phase minimum energy. Negative (positive) valued contour lines are plotted in blue (black) and the zero-valued contour line is shown in red. Green circles indicate the position of the reaction barrier, and barrier heights $E^\dagger$ are also shown.

the H−H and the molecule-surface distances (r, Z) for H_2 approaching Pt(211) with orientations parallel to the surface at different impact sites, and azimuthal orientations as shown in the insets of the figure. As can be seen from Figure 5.4 (a), the dissociation of H_2 proceeds indeed non-activated directly over the top1 site, that is, over a Pt atom at the step edge. Following the colour code of the figure, H_2 can spontaneously dissociate after passing an early, but shallow barrier of $E^\dagger = -83$ meV[1] (barrier is below the classical gas phase minimum) in the entrance channel. The two H atoms are then accommodated exothermally on the surface. This result is in agreement with previous work of McCormack *et al.* [14] where a non-activated route to dissociation was revealed for impacts near the top1 site and with H atoms dissociating to brg1 sites. This result also matches up with the above analysis of the topology of the H on Pt(211) PES that suggested the lowest barrier to be close to the top1 site. Furthermore, the associated barrierless path enables the contribution of a direct non-activated mechanism for reaction at all incidence energies, as found experimentally [8] as well as theoretically [14]. Interestingly, already small changes of the molecular geometry lead to significant changes of the topology of the PES. For example, moving H_2 from the step edge to the bottom of the step while retaining its orientation, as shown in Figure 5.4 (c), yields a 2D-PES that has a large activation barrier of $E^\dagger = 556$ meV and dissociation appears to be endothermic. Aligning now the molecular axis with the X-axis of the surface unit cell, as shown in Figure 5.4 (b), reduces somewhat the barrier but the PES becomes strongly repulsive for very large values of r ($r > 2$ Å). This suggests that the dissociation of H_2 on Pt(211) may be accompanied by a strong angular reorientation dynamics, but also that associative desorption may set in after the molecule has experienced large interatomic stretches.

The different impact sites and initial orientations of the molecule do not only affect how large the barrier toward bond cleavage is and the length of the path towards a favorable adsorption state. They also influence the way in which vibrational and translational energy play in favor of reaction. Throughout the nine plots presented in Figure 5.4, one recognizes the typical elbow form of the PES along the r, Z coordinates. On the one hand, the curvature of the minimum energy paths in the elbows controls the vibration-translation (V-T) coupling [67], which may facilitate dissoci-

[1] $E^\dagger = E_b$

Configuration	$r^\dagger$ [Å]	$Z^\dagger$ [Å]	$E^\dagger$ [eV]
top1 ($\phi = 90°$), Fig.5.4(a)	0.75	2.79	-0.083
top2 ($\phi = 0°$), Fig.5.4(b)	0.90	0.59	0.396
top2 ($\phi = 90°$), Fig.5.4(c)	0.88	0.51	0.556
top3 ($\phi = 90°$), Fig.5.4(i)	1.00	0.99	0.118
brg1 ($\phi = 0°$), Fig.5.4(d)	0.80	1.75	0.186
brg3 ($\phi = 0°$), Fig.5.4(e)	0.94	0.73	0.639
brg4 ($\phi = 30°$), Fig.5.4(h)	1.62	0.75	0.692
brg5 ($\phi = 120°$), Fig.5.4(g)	0.89	1.37	0.318
t2b1 ($\phi = 90°$), Fig.5.4(f)	1.34	1.53	0.035

Table 5.7: Barrier heights and geometries for H_2 on Pt(211) for the geometries shown in Figure 5.4. Energies are given relative to the gas phase minimum energy of H_2.

ation in quasi-classical simulations artificially due to the zero-point energy conversion effect: the higher the curvature, the more coupling. On the other hand, the Polanyi rules [68] relate the efficiency of translational and vibrational excitation of the incident molecule for reaction to the position of the barrier. In late-barrier systems resembling the product state reaction is promoted vibrationally, while in early-barrier systems reaction is more enhanced by translational excitation. For the H_2 + Pt(211) system, vibrationally non-adiabatic V-T processes as well as the Polanyi rules are expected to come into play during the reaction dynamics. For example, we find relatively early barriers for impact situations shown in Figure 5.4 (b)-(d) suggesting a preference of translational excitation for reaction. Impact sites associated with a late barrier are shown in Figure 5.4 (f), (h) and (i). In impacts on these sites, reaction is more likely to be promoted by initial vibrational excitation.

Reaction barrier energies and associated geometries for the nine incidence situations outlined in Figure 5.4 are specified in table 5.7. While the barriers to dissociation could be decreased somewhat when optimized with respect to θ for cases in which H_2 does not dissociate parallel to the step (Figures 5.4 (b), (d), (e), (g), and (h)), Figure 5.4 and table 5.7 nevertheless provide a good view of the H_2-Pt(211) interaction. We find the latest ($r^\dagger$ = 1.62 Å) and highest barrier ($E^\dagger$ = 692 meV) for molecules incident at the brg4 site (see also Figure 5.4 (h)). This indicates a considerable range of

activation energies ($\sim$ 700 meV) for the dissociation process. The $Z^{\dagger}$-values reported in table 5.7 range from 0.51 Å at the top2 site (bottom of the step) to 2.79 Å at the top1 site (top of the step edge). This reflects to some extent the overall shape of the Pt(211) surface, since step-top and step-bottom Pt atoms are displaced by $\Delta Z = 1.27$ Å.

The vdW-DF2 functional employed here yields not only rather large activation energies for the direct dissociation process but also considerable physisorption wells of $\sim$ 72 meV located comparably far away from the surface. The presence of such wells may additionally contribute to the trapping dynamics of small molecules or may even increase the chance of redirecting the molecule toward non-dissociative pathways. Baerends and co-workers [13, 14] previously reported on the importance of trapping as a mechanism for indirect dissociation of H_2 on Pt(211). They used a PES that was constructed on the basis of standard GGA-DFT calculations and the authors found only a shallow physisorption well for impacts at the bottom-step. When using the DF2-functional in the description of the dynamics of molecular hydrogen on Pt(211), as done in this work, the trapping mechanism may become more substantial, which may affect the computation of sticking probabilities for slow molecules.

5.3.2 Comparison QCT and QD dynamics

Figure 5.5 shows the comparison between the QCT and QD results for $H_2(\nu = 0,\ j = 0)$. As already discussed in the introduction, the shape of the reaction probability curve in both the QD and the QCT dynamics arises from the presence of a trapping mechanism, which yields a contribution to the reactivity that decreases with incidence energy, and an activated mechanism, the contribution of which increases with incidence energy. As a result, the reaction of the H_2 molecule on Pt(211) exhibits a nonmonotonic behaviour as a function of the collision energy. The reaction probability curve shows very high dissociation probabilities at very low collision energies. The minimum value of the reaction probability is at an intermediate value of the collision energy and the slope of the reaction probability curve becomes positive at higher collision energies.

As noted by McCormack *et al.* [14], with a GGA PES non-activated indirect dissociation may occur when a molecule hits the lower edge of the step on a non-reactive site, which showed the presence of a shallow chemisorption well in their PES. A difference with our PES is that physisorption can

occur anywhere at the surface, due to the presence of van der Waals wells for the PES computed with the vdW-DF2 correlation functional.

The QCT calculations reproduce the QD results at the higher incidence energies reasonably well. At low and intermediate energies, in the QD results the trapping mechanism manifests itself by the occurrence of peaks in the reaction probabilities, with the peak energies corresponding to the energies of the associated metastable quantum resonance (trapped) states. The comparison suggests that at low and at intermediate energies (up to 0.2 eV) the QCT results tend to overestimate the reactivity a bit. This could be due to two reasons. First, the increase of the reaction probability with decreasing energy at the lower incidence energy is understood to occur as a result of trapping of molecules entering the potential well, in which energy from the motion perpendicular to the surface is transferred into rotation and translational motion parallel to the surface [17]. In the QD calculations trapping should only be due to energy transfer to the motion parallel to the surface [17]. However, classically it is also allowed that energy is transferred from the motion towards the surface to the rotational DOFs [17]. Second, the QCT calculations may suffer from an artificial effect called zero-point-energy (ZPE) leakage, *i.e.*, in QCT calculations the quantization of vibrational energy may be lost and the original vibrational zero point energy may be transferred to other degrees of freedom.

5.3.3 Isotope effects in QCT results for reaction of ($\nu = 0$, $j = 0$) H_2 and D_2

Comparison between the computed QCT reaction probability curves for H_2 and D_2 shows that the reaction probability of H_2 is higher than that of D_2 at the same incidence energy (see Figure 5.6). We attribute this to a zero-point energy effect. H_2 has more energy in zero point vibrational motion than D_2, so there is a higher probability that a given amount of this energy is transferred to motion along the reaction coordinate. Gross and Scheffler [69] for H_2 dissociation on Pd(100) showed that in classical dynamics (no initial zero-point energy) there is no isotope effect between H_2 and D_2 in the sticking probabilities. At first sight, one might expect that steering is less effective for D_2 due to its higher mass and therefore less reaction for D_2 than H_2. On the other hand, D_2 is slower than H_2 at the same kinetic energy, so there is more time for the steering force to redirect the D_2 molecule to a non-activated path. However, they found the quantum

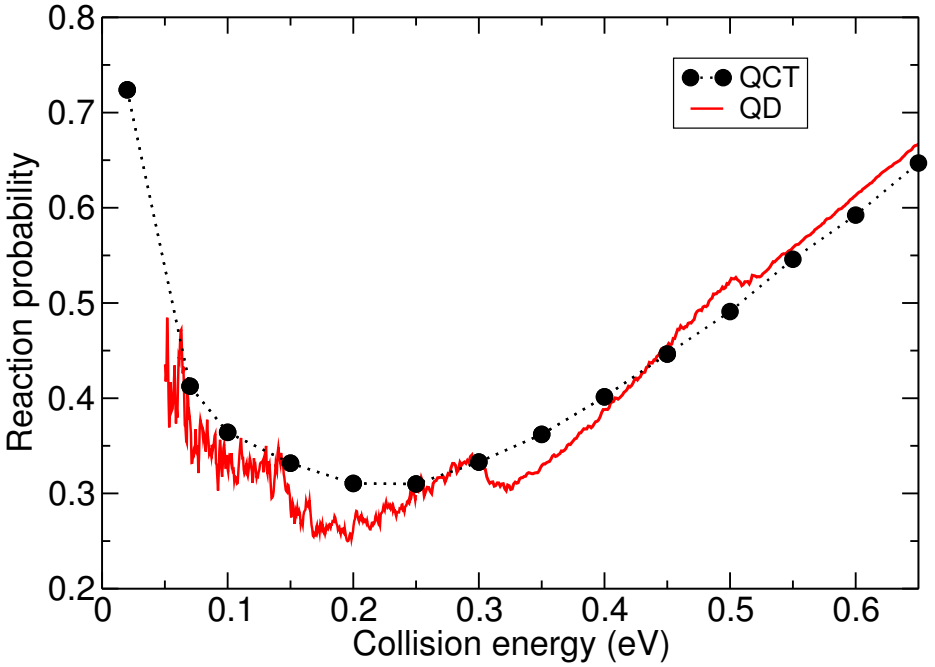

Figure 5.5: Initial-state resolved reaction probability for H_2 ($\nu = 0$, $j = 0$) dissociation on Pt(211) calculated with QD in comparison with the QCT results.

dynamical sticking probabilities of D_2 to be smaller than those of H_2. They suggested that this small difference should be a quantum dynamical effect and that the larger vibrational zero point energy of H_2 can more effectively be used to cross the reaction barrier.

No isotopic dependence and also no surface temperature dependence for the sticking probability were reported by the experimentalists [8], as shown in Figure 5.7 where we show the sticking probability as a function of average incidence energy. (In Ref. [8] the sticking probabilities were shown as a function of the incidence energy corresponding to the most probable energy for a density-weighted incidence energy distribution, see the supporting information of Ref. [63].)

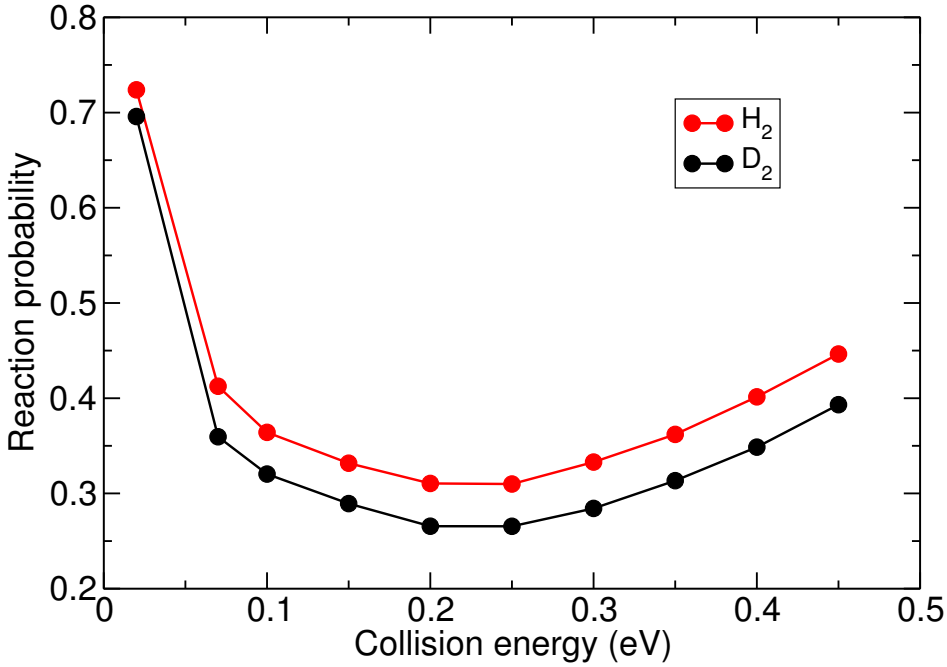

Figure 5.6: Initial-state-resolved reaction probabilities for the dissociation of $H_2(D_2)$ on Pt(211) surface are shown with red (black) symbols for the ground rotational and vibrational state. The results are obtained with the QCT method.

5.3.4 Comparison of molecular beam sticking probabilities with experiment

Parameters used for the molecular beam sticking simulations (previously extracted from experiments as discussed in the supporting information of Ref. [63]) of H_2 and D_2 on Pt(211) are given in table 5.4 and table 5.5 .

The sticking probabilities extracted from molecular beam simulations for H_2 dissociation on Pt(211) are shown in Figure 5.8 with a comparison to the experimental results. In the figure, the red circles show the theoretical results obtained from simulating the experimental beam conditions. The black circles display the experimental results reported by Groot *et al.* [8]. Figure 5.9 shows the same comparison for D_2 dissociation on Pt(211). In both cases, in the lower-energy regime, the theoretical results overestim-

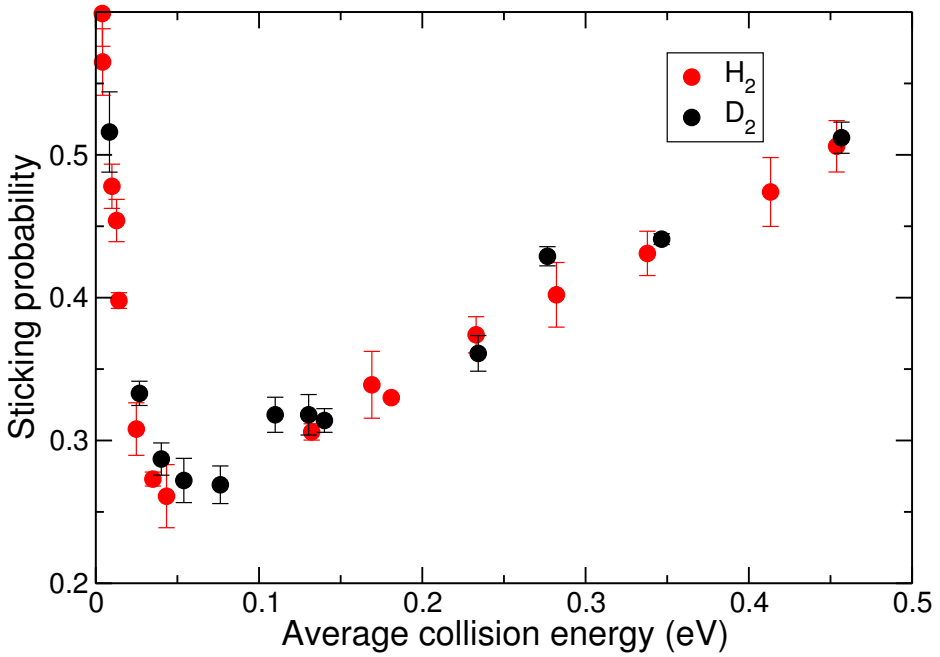

Figure 5.7: The experimental [8] sticking probability of H_2 (red symbols) and D_2 (black symbols) on Pt(211) as a function of average collision energy.

ate the experimental reaction probabilities. For H_2 on Pt(211), at higher energies the theoretical results also overestimate the experimental results. However, overestimation happens only at the highest incidence energy for D_2 + Pt(211). The energy shift (the distance along the energy axis between experimental data points and the interpolated theoretical curve) is [7−92] meV for H_2 + Pt(211) and [3−55] meV for D_2 + Pt(211). On this basis, our results for H_2 + Pt(211) do not yet agree with experiment to within chemical accuracy ($\approx$ 43 meV). To find the mean deviation of the theoretically calculated sticking probability curve from the experimental results, we also calculated the mean absolute error (MAE) and mean signed error (MSE). We obtained a MAE of 40.8 meV and a MSE of 9.8 meV for H_2 and a MAE of 32.4 meV and a MSE of -0.4 meV for D_2. On this basis, the errors in the theoretical data in both cases are less than 1 kcal/mol $\approx$ 43 meV.

As already stated, the comparison between experiment and theoretical results is not yet good at the lower incidence energies. Two reasons might

be involved, which are related to there being an important contribution to sticking from a trapping-mediated mechanism. The first reason concerns the inability of the QCT method to describe the sticking probability accurately when trapping contributes to reaction. The QCT results overestimate the contribution of trapping due to translation-to-rotation energy transfer, which is not allowed in QD descriptions [70] (see Section 5.3.2). The quantum dynamics calculations of Figure 5.5 suggest that for reaction of $H_2(\nu = 0, j = 0)$ the reaction probability decreases faster with energy at low incidence energies if quantum effects are included, which goes in the right direction for getting better agreement with experiment. The other effect that could be important is surface temperature, which we do not include in our calculations. The initial reaction probability was experimentally determined at the surface temperature of 300 K. However, the experimentalists did not observe any surface temperature dependence [8]. In our view this makes it unlikely that the static surface approximation we used here is responsible for the discrepancy with experiment at low incidence energy.

Especially for H_2 our QCT results overestimate the experimental sticking probability at high average energies, as computed from the beam parameters available from fitting experimental TOF spectra (see the supporting information of Ref. [63]). One question we addressed is whether this could be due to errors arising from fitting these parameters, which is critically difficult especially at high incidence energies associated with short flight times. Now it is rather well known that for pure H_2 beams the average translational energy should not exceed 2.7 $k_B T_n$, as no vibrational cooling occurs, and only about 20% rotational cooling [62, 71, 72]. Comparing the average incidence energies of the pure H_2 beams in table 5.4 with 2.7 $k_B T_n$, we however find that in most cases the average incidence energies exceed 3 $k_B T_n$, and this also holds true for pure D_2 beams (see also table 5.5). This suggests that the experimental average incidence energies extracted from the beam parameters were too high. By re-plotting the experimental results using average incidence energies E_{corr} equal to 2.7 $k_B T_n$ we can redo the comparison with the computed sticking probabilities, if we assume that the computed values do not much depend on the nozzle temperature through altered ro-vibrational state distributions. This is likely to hold true for non-activated or weakly activated dissociation. As Figure 5.10 shows this approach tremendously improves the agreement with experiment for the higher incidence energies at which the sticking is dominated by activated dissociation, and for which the QCT results should be accurate (see Sec-

tion 5.3.2): The agreement with experiment is now within chemical accuracy for these energies and pure H_2 beam conditions. For D_2 the agreement is not as good as for H_2 for the lower incidence energies in the high-energy range (see Figure 5.11), which is perhaps due to the rotational cooling being somewhat more efficient for D_2 than for H_2, due to the lower rotational constant of D_2. This means that in Figure 5.11 the experimental data could move somewhat to the right (to higher energies), thereby improving the agreement with experiment. Note also that in principle the fits of the beam parameters are expected to be less error prone for H_2 than for D_2, due to longer flight times of D_2.

Another solution to the puzzle of why the average incidence energies calculated from the beam parameters did not correspond to 2.7 $k_B T_n$ for pure beams could be that the nozzle temperature was actually higher than measured. This could in principle be simulated by assuming that the nozzle temperature can be computed from the measured average incidence energy, instead of adapting the average incidence energy to the measured nozzle temperature. This was not pursued computationally, as it would only be expected to lead to a small increase of the computed sticking probability, and to somewhat larger discrepancies for H_2 + Pt(211), for which the agreement with experiment was worst to start with.

Above, we have suggested that the rotational cooling in a D_2 beam could be somewhat more efficient than in the H_2 beam (due to the rotational constant of D_2 being lower). If this were true, this would suggest that we could have plotted the experimental data for the pure D_2 beams as a function of $\langle E_i \rangle = c k_B T_n$ with c somewhat larger than 2.7 (for instance, 2.75 or 2.8) in Figure 5.11. If this would be correct, this would increase the agreement between theory and experiment in this figure, as already discussed above. However, it should also alter the conclusion regarding the absence of an isotope effect drawn originally by the experimentalists: if this assumption would be correct, the sticking probabilities measured for H_2 should be somewhat higher than those for D_2, at least for the results from the pure H_2 and pure D_2 experiments. This would bring theory and experiment in agreement also regarding the qualitative conclusion on the isotope effect.

5.3.5 Comparison MD and MDEF results for sticking

Figures 5.12 and 5.13 show the results of MD and MDEF calculations for H_2 + Pt(211) and D_2 + Pt(211). At low energies adding electronic fric-

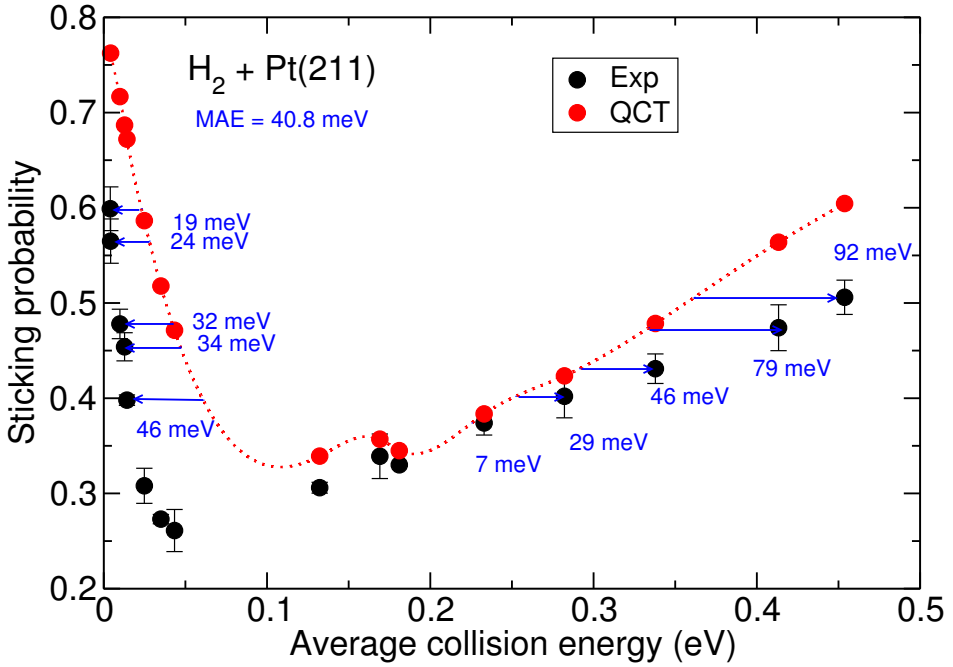

Figure 5.8: Sticking probability for molecular beam of H_2 on Pt(211) simulated with QCT. For comparison experimental results reported by Groot *et al.* (Black symbols: experimental data from Ref. [8]) are plotted beside the theoretical results (red symbols). The arrows and accompanying numbers show the collision energy difference between the interpolated theoretical results and experimental data.

tion and doubling the friction coefficient increases the sticking probability for D_2. Doubling the electronic friction coefficient increases the sticking probabilities of H_2 only at intermediate energies. At higher incidence energies adding electronic friction decreases the sticking probability a little bit. Adding this energy dissipation channel reduces sticking somewhat at higher incidence energies because energy in the bond stretch coordinate is nonadiabatically dissipated to electron-hole pair excitation. Also modeling the effect of the finite electronic temperature decreases the sticking probability at lower incidence energies, but there is no dramatic effect at higher incidence energies. The effect of T_{el} is negligible for $\langle E_i \rangle > 0.13$ eV and very small at lower incidence energy. At the lowest incidence energies, the

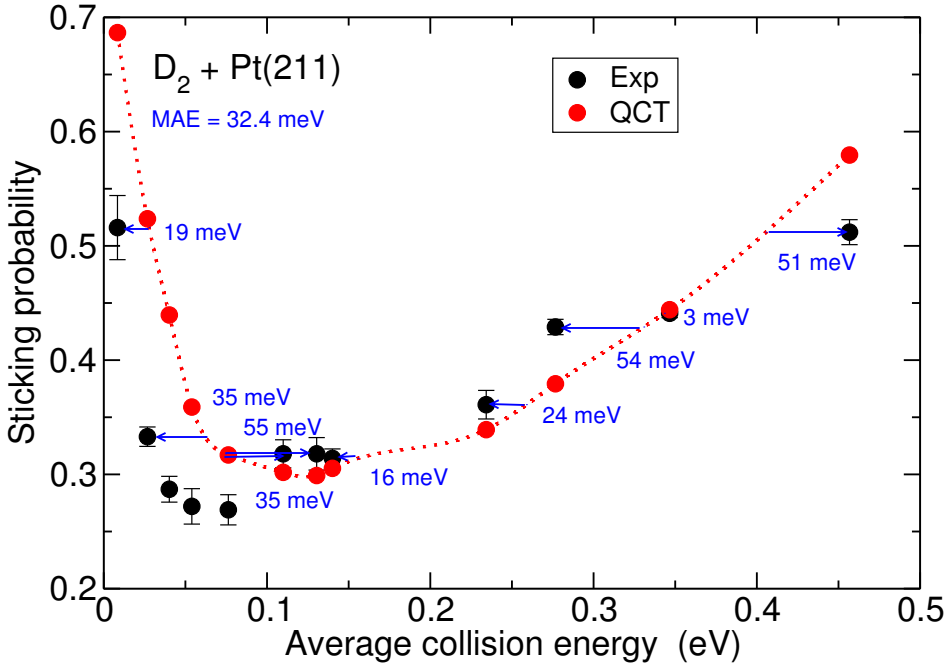

Figure 5.9: Sticking probability for molecular beam of D_2 on Pt(211) simulated with QCT. For comparison experimental results reported by Groot *et al.* (Black symbols: experimental data from Ref. [8]) are plotted beside the theoretical results (red symbols). The arrows and accompanying numbers show the collision energy difference between the interpolated theoretical results and experimental data.

electronic dissipative channel enhances the trapping and, therefore, the dissociation probability [73]. The dissociation process is expected to increase in the presence of a trapping mechanism because once the molecule is trapped on the surface and starts to dissipate energy, it is difficult for the trapped molecule to recover the perpendicular translational energy to escape from the surface. The effect of including electron-hole pair excitations is therefore to increase the trapping-mediated contribution to the reactivity and thereby the reactivity. However, it keeps the direct mechanism almost unchanged. Raising the electronic temperature at lower incidence energies, *i.e.* through the presence of hot electrons, leads to collisions of the hot electrons with the molecule that can excite the molecular DOFs and provide the trapped mo-

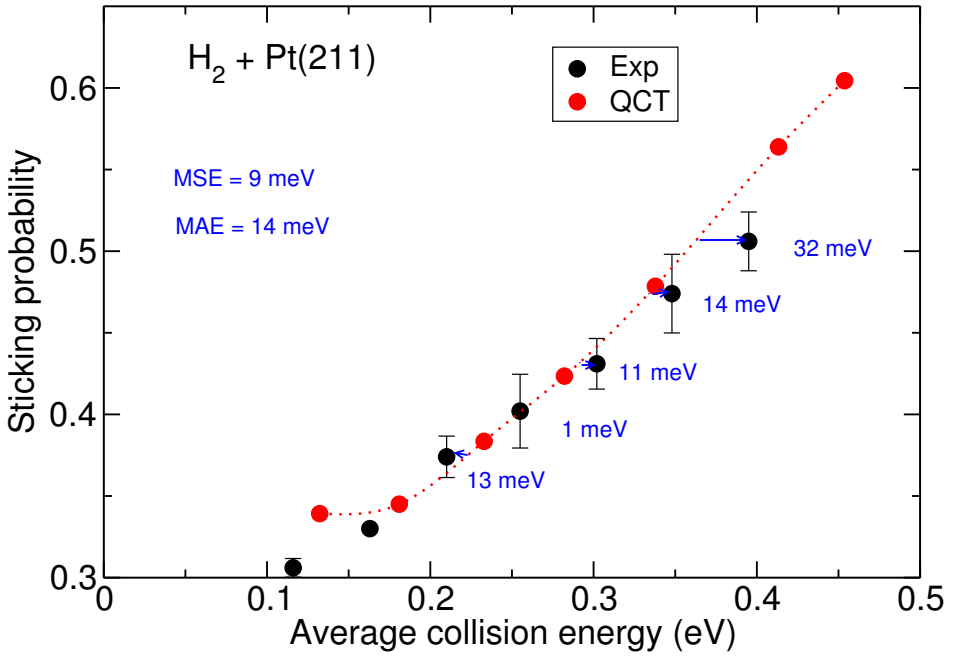

Figure 5.10: Sticking probability for molecular beam of H_2 on Pt(211) simulated with QCT. For comparison experimental results reported by Groot *et al.* (Black symbols: experimental data from Ref. [8].) are plotted beside the theoretical results (red symbols). The arrows and accompanying numbers show the collision energy difference between the interpolated theoretical results and experimental data. In plotting the experimental results, we have assumed that the average incidence energy in the experiments was equal to 2.7 $k_B T_n$.

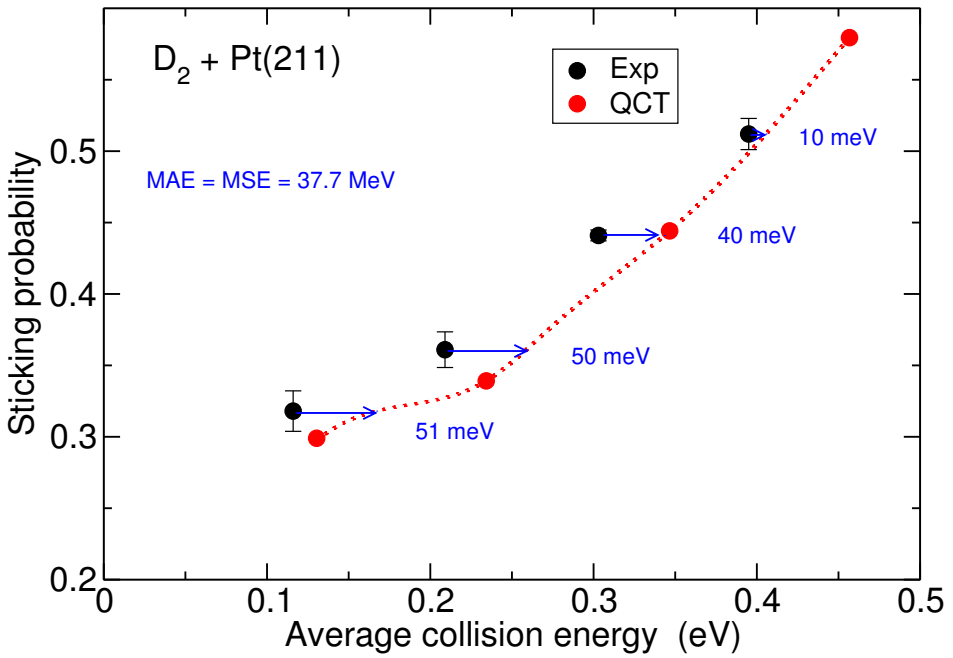

Figure 5.11: Sticking probability for molecular beam of D_2 on Pt(211) simulated with QCT. For comparison experimental results reported by Groot *et al.* (Black symbols: experimental data from Ref. [8].) are plotted beside the theoretical results (red symbols). The arrows and accompanying numbers show the collision energy difference between the interpolated theoretical results and experimental data. In plotting the experimental results, we have assumed that the average incidence energy in the experiments was equal to 2.7 $k_B T_n$.

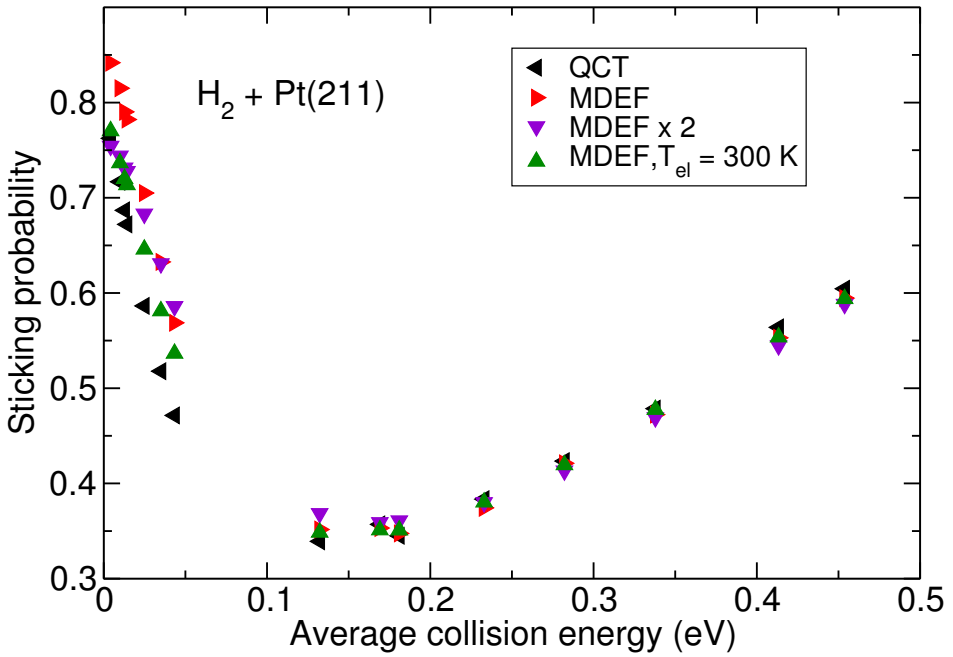

Figure 5.12: Sticking probability as a function of the average incidence energy obtained from MD and MDEF calculations. Black symbols show the MD, red and purple symbols show results of MDEF calculations using friction coefficient multiplied by different factors ($\times$ 1 and $\times$ 2 respectively) and green symbols show MDEF results using an electronic temperature $T_{el} = 300$ K.

lecule with sufficiently high energy to get desorbed from the surface to the gas phase. Taking the electronic temperature in our calculations at lower incidence energies into account diminishes the trapping effect and therefore reduces the overall reactivity.

The good agreement between the MD and MDEF results at higher incidence energies confirms that the BOSS model, which does not consider electron-hole pair excitation, may accurately describe the dissociation of H_2 and D_2 on Pt(211) through the direct reaction mechanism at the terrace, and therefore, at higher incidence energies.

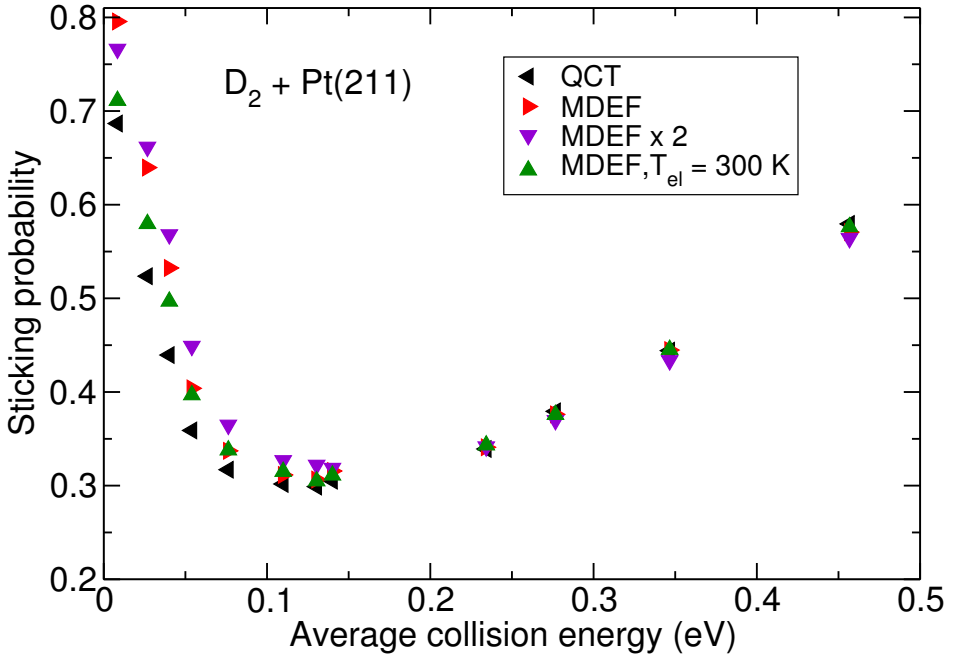

Figure 5.13: Sticking probability as a function of the average incidence energy obtained from MD and MDEF calculations. Black symbols show the MD, red and purple symbols show results of MDEF calculations using friction coefficient multiplied by different factors ($\times$ 1 and $\times$ 2 respectively) and green symbols show MDEF results using an electronic temperature $T_{el} = 300$ K.

5.4 Conclusion

To address the question whether the SRP−DF functional derived for the H_2 + Pt(111) is transferable to the H_2 + Pt(211) system, we have performed calculations on the dissociation of H_2/D_2 on the stepped Pt(211) surface. We used the VASP software package to compute the raw DFT data. The CRP interpolation method was used to accurately fit these data and construct the 6D PES based on the PBEα-vdW-DF2 functional with α set to 0.57. The potential energy for H on Pt(211) for geometry optimized atom-surface distances on a (1×1) supercell was discussed and was compared with the previously developed PES of Olsen *et al.* [42] . We have also

discussed features of the PES for H_2 dissociation on Pt(211) and reported on minimum barrier heights and associated geometries.

We have performed calculations within the BOSS model and within the MDEF model, in order to study non-adiabatic effects on the dissociation dynamics due to the creation of electron-hole pairs in the surface. The QCT method has been used to compute the initial-state resolved reaction probability and molecular beam sticking probability. The initial-state resolved reaction probability results obtained with the QCT method were compared with the results of QD calculations. The QCT calculations reproduced the QD results at the high energy range but not at the low energy range. The discrepancy between the results of these two dynamics methods at the low energy regime was discussed. We have also shown and discussed the isotope effect in the QCT results on the reaction probability of $(\nu = 0, j = 0)$ of H_2 and D_2.

We have computed the sticking probabilities of molecular hydrogen and deuterium on Pt(211) and compared our theoretical results with the experimental data. Our theoretical results showed that the reactivity on Pt(211) is enhanced relative to Pt(111), in agreement with experiment. The lowest barrier height for reaction was found at the upper edge of the step. Reaction on the upper edge of the step is not activated. We have simulated molecular beam sticking probabilities and compared them with the experimental data of Groot *et al.* [8]. We have reported the energy shifts between the experimental data and the spline-interpolated theoretical data to be in this range [7−92] meV for H_2 + Pt(211) and [3−55] meV for D_2 + Pt(211). Thus, in this sense chemical accuracy was not yet achieved in our theoretical results. However, it is well-known that the average energy of pure H_2 beams should not exceed 2.7 $k_B T_n$ due to the absence of vibrational cooling and the occurrence of only about 20% rotational cooling for a pure beam. Nevertheless, we found that in most cases the average energies of the pure H_2 and the pure D_2 beams exceeded 3 $k_B T_n$. Consequently, we have re-plotted the experimental results employing average energies equal to 2.7 $k_B T_n$ and re-done the comparison with computed sticking probabilities. With this modification, the agreement between experiment and theory tremendously improved for H_2. The agreement between theory and experiment for D_2 was not as satisfactory as for H_2 at the lower incidence energies in the high energy range. These results suggest that the experiments should be repeated and be reported for more accurately measured beam parameters to enable a better determination of the accuracy of the theoretical results.

Finally, we have presented the comparison of MD and MDEF results for the sticking probability for both H_2 and D_2 and discussed the effect of adding electronic friction and doubling the friction coefficient, and the effect of electronic temperature on the sticking at low and high incidence energies.

References

1. Zambelli, T., Wintterlin, J., Trost, J. & Ertl, G. Identification of the "Active Sites" of a Surface-Catalyzed Reaction. *Science* **273,** 1688–1690 (1996).

2. Lu, K. & Rye, R. Flash Desorption and Equilibration of H_2 and D_2 on Single Crystal Surfaces of Platinum. *Surface Science* **45,** 677–695 (1974).

3. Bernasek, S. L. & Somorjai, G. A. Molecular Beam Study of the Mechanism of Catalyzed Hydrogen–Deuterium Exchange on Platinum Single Crystal Surfaces. *Journal of Chemical Physics* **62,** 3149–3161 (1975).

4. Christmann, K. & Ertl, G. Interaction of Hydrogen with Pt(111): The Role of Atomic Steps. *Surface Science.* **60,** 365–384 (1976).

5. Poelsema, B., Mechtersheimer, G. & Comsa, G. The Interaction of Hydrogen with Platinum(s)-9(111) × (111) Studied with Helium Beam Diffraction. *Surface Science* **111,** 519–544 (1981).

6. Gee, A. T., Hayden, B. E., Mormiche, C. & Nunney, T. S. The Role of Steps in the Dynamics of Hydrogen Dissociation on Pt(533). *Journal of Chemical Physics* **112,** 7660–7668 (2000).

7. Groot, I. M. N., Schouten, K. J. P., Kleyn, A. W. & Juurlink, L. B. F. Dynamics of Hydrogen Dissociation on Stepped Platinum. *Journal of Chemical Physics* **129,** 224707 (2008).

8. Groot, I. M. N., Kleyn, A. W. & Juurlink, L. B. F. The Energy Dependence of the Ratio of Step and Terrace Reactivity for H_2 Dissociation on Stepped Platinum. *Angewandte Chemie International Edition* **50,** 5174–5177 (2011).

9. Dahl, S. *et al.* Role of Steps in N_2 Activation on Ru(0001). *Physics Review Letters* **83,** 1814–1817 (1999).

10. Honkala, K. *et al.* Ammonia Synthesis from First-Principles Calculations. *Science* **307,** 555–558 (2005).

11. Gee, A. T., Hayden, B. E., Mormiche, C., Kleyn, A. W. & Riedmüller, B. The Dynamics of the Dissociative Adsorption of Methane on Pt(533). *Journal of Chemical Physics* **118,** 3334–3341 (2003).

12. Migliorini, D. *et al.* Surface Reaction Barriometry: Methane Dissociation on Flat and Stepped Transition-Metal Surfaces. *Journal of Physical Chemistry Letters* **8,** 4177–4182 (2017).

13. Olsen, R., McCormack, D. & Baerends, E. How Molecular Trapping Enhances the Reactivity of Rough Surfaces. *Surface Science* **571,** L325–L330 (2004).

14. McCormack, D. A., Olsen, R. A. & Baerends, E. J. Mechanisms of H_2 Dissociative Adsorption on the Pt(211) Stepped Surface. *Journal of Chemical Physics* **122,** 194708 (2005).

15. Luppi, M., McCormack, D. A., Olsen, R. A. & Baerends, E. J. Rotational Effects in the Dissociative Adsorption of H_2 on the Pt(211) Stepped Surface. *Journal of Chemical Physics* **123,** 164702 (2005).

16. Ludwig, J., Vlachos, D. G., van Duin, A. C. T. & Goddard, W. A. Dynamics of the Dissociation of Hydrogen on Stepped Platinum Surfaces using the ReaxFF Reactive Force Field. *Journal of Physical Chemistry B* **110,** 4274–4282 (2006).

17. Olsen, R. A., McCormack, D. A., Luppi, M. & Baerends, E. J. Six-Dimensional Quantum Dynamics of H_2 Dissociative Adsorption on the Pt(211) Stepped Surface. *Journal of Chemical Physics* **128,** 194715 (2008).

18. Füchsel, G. *et al.* Anomalous Dependence of the Reactivity on the Presence of Steps: Dissociation of D_2 on Cu(211). *Journal of Physical Chemistry Letters* **9,** 170–175 (2018).

19. Cao, K., Füchsel, G., Kleyn, A. W. & Juurlink, L. B. F. Hydrogen Adsorption and Desorption from Cu(111) and Cu(211). *Physical Chemistry Chemical Physics* **20,** 22477–22488 (2018).

20. Huang, X., Yan, X. & Xiao, Y. Effects of Vacancy and Step on Dissociative Dynamics of H_2 on Pd(111) Surfaces. *Chemical Physics Letters* **531,** 143–148 (2012).

21. Fuhrmann, T. *et al.* Activated Adsorption of Methane on Pt(111) -an in Situ XPS Study. *New Journal of Physics* **7,** 107 (2005).

22. Chadwick, H., Gutièrrez-Gonzàlez, A., Migliorini, D., Beck, R. D. & Kroes, G. J. Incident Angle Dependence of CHD_3 Dissociation on the Stepped Pt(211) Surface. *Journal of Physical Chemistry C* **122,** 19652–19660 (2018).

23. Chadwick, H. *et al.* Methane Dissociation on the Steps and Terraces of Pt(211) Resolved by Quantum State and Impact Site. *Journal of Chemical Physics* **148,** 014701 (2018).

24. Migliorini, D., Chadwick, H. & Kroes, G. J. Methane on a Stepped Surface: Dynamical Insights on the Dissociation of CHD_3 on Pt(111) and Pt(211). *Journal of Chemical Physics* **149,** 094701 (2018).

25. Díaz, C. *et al.* Chemically Accurate Simulation of a Prototypical Surface Reaction: H_2 Dissociation on Cu(111). *Science* **326,** 832–834 (2009).

26. Sementa, L. *et al.* Reactive Scattering of H_2 from Cu(100): Comparison of Dynamics Calculations Based on the Specific Reaction Parameter Approach to Density Functional Theory with Experiment. *Journal of Chemical Physics* **138** (2013).

27. Nattino, F. *et al.* Chemically Accurate Simulation of a Polyatomic Molecule-Metal Surface Reaction. *Journal of Physical Chemistry Letters* **7,** 2402–2406 (2016).

28. Ghassemi, E. N., Wijzenbroek, M., Somers, M. F. & Kroes, G. J. Chemically Accurate Simulation of Dissociative Chemisorption of D_2 on Pt(111). *Chemical Physics Letters* **683.** Ahmed Zewail (1946-2016) Commemoration Issue of Chemical Physics Letters, 329–335 (2017).

29. Becke, A. D. Density-Functional Exchange-Energy Approximation with Correct Asymptotic Behavior. *Physical Review A* **38,** 3098–3100 (1988).

30. Perdew, J. P. Density-Functional Approximation for the Correlation Energy of the Inhomogeneous Electron Gas. *Physical Review B* **33,** 8822–8824 (1986).

31. Busnengo, H. F., Salin, A. & Dong, W. Representation of the 6D Potential Energy Surface for a Diatomic Molecule Near a Solid Surface. *Journal of Chemical Physics* **112,** 7641–7651 (2000).

32. Groot, I. M. N., Kleyn, A. W. & Juurlink, L. B. F. Separating Catalytic Activity at Edges and Terraces on Platinum: Hydrogen Dissociation. *Journal of Physical Chemistry C* **117,** 9266–9274 (2013).

33. Kresse, G. & Hafner, J. *Ab Initio* Molecular Dynamics for Liquid Metals. *Physical Review B* **47,** 558–561 (1993).

34. Kresse, G. & Hafner, J. *Ab Initio* Molecular-Dynamics Simulation of the Liquid-Metal-Amorphous-Semiconductor Transition in Germanium. *Physical Review B* **49,** 14251–14269 (1994).

35. Kresse, G. & Furthmüller, J. Efficiency of *Ab-Initio* Total Energy Calculations for Metals and Semiconductors Using a Plane-Wave Basis Set. *Computational Materials Science* **6,** 15–50 (1996).

36. Kresse, G. & Furthmüller, J. Efficient Iterative Schemes for *Ab Initio* Total-Energy Calculations Using a Plane-Wave Basis Set. *Physical Review B* **54,** 11169–11186 (1996).

37. Madsen, G. K. H. Functional Form of the Generalized Gradient Approximation for Exchange: The PBEα Functional. *Physical Review B* **75,** 195108 (2007).

38. Lee, K., Murray, É. D., Kong, L., Lundqvist, B. I. & Langreth, D. C. Higher-Accuracy van der Waals Density Functional. *Physical Review B* **82,** 081101 (2010).

39. Luntz, A. C., Brown, J. K. & Williams, M. D. Molecular Beam Studies of H_2 and D_2 Dissociative Chemisorption on Pt(111). *Journal of Chemical Physics* **93,** 5240–5246 (1990).

40. Monkhorst, H. J. & Pack, J. D. Special Points for Brillouin-Zone Integrations. *Physical Review B* **13,** 5188–5192 (1976).

41. Materer, N. *et al.* Reliability of Detailed LEED Structural Analyses: Pt(111) and Pt(111)-p(2×2)-O. *Surface Science* **325,** 207–222 (1995).

42. Olsen, R. A., Bădescu,. C., Ying, S. C. & Baerends, E. J. Adsorption and Diffusion on a Stepped Surface: Atomic Hydrogen on Pt(211). *Journal of Chemical Physics* **120,** 11852–11863 (2004).

43. Karplus, M., Porter, R. N. & Sharma, R. D. Exchange Reactions with Activation Energy. I. Simple Barrier Potential for (H, H_2). *Journal of Chemical Physics* **43,** 3259–3287 (1965).

44. Füchsel, G., del Cueto, M., Díaz, C. & Kroes, G. J. Enigmatic HCl + Au(111) Reaction: A Puzzle for Theory and Experiment. *Journal of Physical Chemistry C* **120,** 25760–25779 (2016).

45. Head-Gordon, M. & Tully, J. C. Molecular Dynamics with Electronic Frictions. *Journal of Chemical Physics* **103,** 10137–10145 (1995).

46. Lemons, D. S. & Gythiel, A. Paul Langevin's 1908 paper "On the Theory of Brownian Motion" ["Sur la théorie du mouvement brownien," C. R. Acad. Sci. (Paris) 146, 530-533 (1908)]. *American Journal of Physics* **65,** 1079–1081 (1997).

47. Füchsel, G., Klamroth, T., Monturet, S. & Saalfrank, P. Dissipative Dynamics within the Electronic Friction Approach: the Femtosecond Laser Desorption of H_2/D_2 from Ru(0001). *Physical Chemistry Chemical Physics* **13,** 8659–8670 (2011).

48. Juaristi, J. I., Alducin, M., Muiño, R. D., Busnengo, H. F. & Salin, A. Role of Electron-Hole Pair Excitations in the Dissociative Adsorption of Diatomic Molecules on Metal Surfaces. *Physical Review Letters* **100,** 116102 (2008).

49. Novko, D., Blanco-Rey, M., Alducin, M. & Juaristi, J. I. Surface Electron Density Models for Accurate *Ab Initio* Molecular Dynamics with Electronic Friction. *Physical Review B* **93,** 245435 (2016).

50. Puska, M. J. & Nieminen, R. M. Atoms Embedded in an Electron Gas: Phase Shifts and Cross Sections. *Physical Review B* **27,** 6121–6128 (1983).

51. Füchsel, G., Schimka, S. & Saalfrank, P. On the Role of Electronic Friction for Dissociative Adsorption and Scattering of Hydrogen Molecules at a Ru(0001) Surface. *Journal of Physical Chemistry A* **117,** 8761–8769 (2013).

52. Luntz, A. C. *et al.* Comment on "Role of Electron-Hole Pair Excitations in the Dissociative Adsorption of Diatomic Molecules on Metal Surfaces". *Physical Review Letters* **102,** 109601 (2009).

53. Spiering, P. & Meyer, J. Testing Electronic Friction Models: Vibrational De-Excitation in Scattering of H_2 and D_2 from Cu(111). *Journal of Physical Chemistry Letters* **9,** 1803–1808 (2018).

54. Maurer, R. J., Jiang, B., Guo, H. & Tully, J. C. Mode Specific Electronic Friction in Dissociative Chemisorption on Metal Surfaces: H_2 on Ag(111). *Physical Review Letters* **118,** 256001 (2017).

55. Kosloff, R. Time-Dependent Quantum-Mechanical Methods for Molecular Dynamics. *Journal of Physical Chemistry* **92,** 2087–2100 (1988).

56. Pijper, E., Kroes, G. J., Olsen, R. A. & Baerends, E. J. Reactive and Diffractive Scattering of H_2 from Pt(111) Studied Using a Six-Dimensional Wave Packet Method. *Journal of Chemical Physics* **117,** 5885–5898 (2002).

57. Feit, M., Fleck, J. & Steiger, A. Solution of the Schrödinger Equation by a Spectral Method. *Journal of Computational Physics* **47,** 412–433 (1982).

58. Vibok, A. & Balint-Kurti, G. G. Parametrization of Complex Absorbing Potentials for Time-Dependent Quantum Dynamics. *Journal of Physical Chemistry* **96,** 8712–8719 (1992).

59. Corey, G. C. & Lemoine, D. Pseudospectral Method for Solving the Time–Dependent Schrödinger Equation in Spherical Coordinates. *Journal of Chemical Physics* **97,** 4115–4126 (1992).

60. Lemoine, D. The Finite Basis Representation as the Primary Space in Multidimensional Pseudospectral Schemes. *Journal of Chemical Physics* **101,** 10526–10532 (1994).

61. Balint-Kurti, G. G., Dixon, R. N. & Marston, C. C. Grid Methods for Solving the Schrödinger Equation and Time Dependent Quantum Dynamics of Molecular Photofragmentation and Reactive Scattering Processes. *International Reviews in Physical Chemistry* **11,** 317–344 (1992).

62. Rettner, C. T., Michelsen, H. A. & Auerbach, D. J. Quantum-State-Specific Dynamics of the Dissociative Adsorption and Associative Desorption of H_2 at a Cu(111) Surface. *Journal of Chemical Physics* **102,** 4625–4641 (1995).

63. Ghassemi, E. N. *et al.* Transferability of the Specific Reaction Parameter Density Functional for H_2 + Pt(111) to H_2 + Pt(211). *Journal of Physical Chemistry C* **123,** 2973–2986 (2019).

64. Ermak, D. L. & Buckholz, H. Numerical Integration of the Langevin Equation: Monte Carlo Simulation. *Journal of Computational Physics* **35,** 169–182 (1980).

65. Winkler, A. Interaction of Atomic Hydrogen with Metal Surfaces. *Applied Physics A* **67,** 637–644 (1998).

66. Kroes, G. J., Pavanello, M., Blanco-Rey, M., Alducin, M. & Auerbach, D. J. *Ab Initio* Molecular Dynamics Calculations on Scattering of Hyperthermal H Atoms from Cu(111) and Au(111). *Journal of Chemical Physics* **141,** 054705 (2014).

67. Darling, G. R. & Holloway, S. Translation-to-Vibrational Excitation in the Dissociative Adsorption of D_2. *Journal of Chemical Physics* **97,** 734–736 (1992).

68. Polanyi, J. C. Concepts in Reaction Dynamics. *Accounts of Chemical Research* **5,** 161–168 (1972).

69. Gross, A. Reactions at Surfaces Studied by *Ab Initio* Dynamics Calculations. *Surface Science Reports* **32,** 291–340 (1998).

70. Busnengo, H. F. *et al.* Six-Dimensional Quantum and Classical Dynamics Study of $H_2(\nu = 0, J = 0)$ Scattering from Pd(111). *Chemical Physics Letters* **356,** 515–522 (2002).

71. Gallagher, R. J. & Fenn, J. B. Rotational Relaxation of Molecular Hydrogen. *Journal of Chemical Physics* **60,** 3492–3499 (1974).

72. Rendulic, K., Anger, G. & Winkler, A. Wide Range Nozzle Beam Adsorption Data for the Systems H_2/Nickel and H_2/Pd(100). *Surface Science* **208,** 404–424 (1989).

73. Goikoetxea, I., Juaristi, J. I., Alducin, M. & Muiño, R. D. Dissipative Effects in the Dynamics of N_2 on Tungsten Surfaces. *Journal of Physical Condense Matter* **21,** 264007 (2009).